

The first 3D MHD core-collapse progenitors II: Rotation, magnetic-field amplification, and magnetic topology

A. Griffiths^{1,2}, Miguel-Á. Aloy^{1,3}, and M. Obergaulinger^{1,3}

¹ Departament d'Astronomia i Astrofísica, Universitat de València, 46100 Burjassot, Spain

² Astrophysics Group, Lennard-Jones Laboratories, Keele University, Keele ST5 5BG, UK
e-mail: a.griffiths@keele.ac.uk, miguel.a.aloy@uv.es

³ Observatori Astronòmic, Universitat de València, 46980 Paterna, Spain

Received September 30, 20XX

ABSTRACT

Context. The most energetic core-collapse supernovae are thought to arise from rapidly rotating, magnetised progenitors. However, the three-dimensional pre-collapse structure of their angular momentum and magnetic fields remains poorly constrained, limiting the realism of magnetorotational core-collapse simulations.

Aims. We investigate the angular-momentum distribution, magnetic-field amplification and magnetic topology of physically consistent three-dimensional magnetohydrodynamic pre-supernova progenitors. This second paper focuses on the rotational and magnetic properties of the models introduced in [Paper I](#).

Methods. We used Aenus-ALCAR to evolve two compact Wolf-Rayet progenitors, computed with the stellar-evolution codes GENEC and MESA, through the final minutes before core collapse. The initial magnetic-field strengths were derived from the one-dimensional stellar-evolution prescriptions in radiative regions and then evolved self-consistently in three dimensions.

Results. Our models suggest that the rotation profile near the inner core can depart from a purely shellular distribution and reorganise toward a more cylindrical structure. In convective regions, hydrodynamic Reynolds stresses drive the flow toward an approximately constant specific-angular-momentum profile, corresponding to an average rotation profile close to $\Omega \propto \varpi^{-2}$ (ϖ denotes the cylindrical radius). Maxwell stresses oppose this tendency but are not strong enough in our models to restore rigid rotation. Convective regions amplify seed magnetic fields, transported from neighbouring radiative layers, producing saturated fields with comparable toroidal and poloidal components and a topology containing substantial small-scale power. As a result, regions that are magnetically disconnected in the original one-dimensional stellar-evolution description become magnetically linked in the multidimensional models. Together with [Paper I](#), these models represent the first 3D MHD pre-supernova progenitors of this kind, suitable for subsequent collapse and explosion calculations.

Conclusions. Multidimensional evolution can substantially modify both the angular-momentum distribution and magnetic topology of pre-collapse progenitors. They provide a physically motivated basis for constructing more realistic initial conditions for magnetorotational core-collapse simulations and for improving prescriptions of magneto-convective angular-momentum transport in late stellar evolution.

Key words. stars: massive – stars: rotation – stars: magnetic field – magnetohydrodynamics (MHD) – convection – supernovae: general

1. Introduction

Massive stars with rapid rotation and strong magnetic fields are leading candidates for the progenitors of the most energetic core-collapse supernova (CCSNe), including hypernovae and some long gamma-ray bursts (e.g. [Woosley & Bloom 2006](#); [Nomoto et al. 2007](#); [Burrows et al. 2007](#); [Müller 2024](#)). Magnetorotational explosions have also been proposed as favourable sites for the production of heavy *r*-process nuclei (e.g. [Reichert et al. 2022](#); [Zha et al. 2024](#)), and their nucleosynthetic yields can depend sensitively on the strength and topology of the progenitor magnetic field ([Reichert et al. 2024](#)). The angular-momentum (AM) and magnetic-field distributions in the stellar core are therefore central ingredients for predicting the explosion geometry, the compact-remnant spin, and the magnetic-field structure inherited by the nascent neutron star.

Current magnetorotational CCSN calculations are usually initialised from one-dimensional stellar-evolution (SE) models (e.g. [Mösta et al. 2014](#); [Obergaulinger & Aloy 2020](#)). Such

models can only estimate magnetic-field strengths in radiative regions through effective prescriptions for magnetic instabilities, such as the Tayler-Spruit (TS) dynamo ([Spruit 2002](#)) or, in some cases, the magneto-rotational instability (MRI; [Balbus & Hawley 1991](#)). However, they do not provide the global three-dimensional (3D) geometry of the field, nor the magnetic connectivity amongst the iron core, radiative layers, and convective shells. This limitation is particularly important because multidimensional simulations of magnetorotational explosions have shown that the field topology, not only its amplitude, can influence the explosion dynamics and outcome (e.g. [Obergaulinger & Aloy 2017](#); [Aloy & Obergaulinger 2021](#); [Bugli et al. 2021](#)).

Existing multidimensional MHD studies have begun to clarify the role of convective burning shells in magnetic-field amplification and AM transport (e.g. [Varma & Müller 2021](#); [Varma et al. 2023](#)). However, they do not yet provide whole-star, self-consistent, rotating and magnetised pre-collapse progenitors

extending from the iron core to the outer stellar layers—in particular, excising the core precludes determining how the magnetic flux connects the inner regions to the overlying convective shells, and how the resulting field topology would be inherited by the collapsing core.

Beyond their use as initial conditions for CCSNe simulations, multidimensional MHD progenitor models can also provide feedback for SE modelling. Stellar-evolution calculations necessarily rely on effective one-dimensional prescriptions for convection, AM transport, and magnetic stresses. The companion paper of this series (Griffiths et al. 2026a, hereafter Paper I) focused on convection and nuclear burning in the final pre-collapse shells. In the present paper (Paper II, hereafter) we address the complementary problem: the evolution of rotation, magnetic-field amplification, and magnetic topology during the final minutes before collapse. Related work on magnetised stellar interiors has often focused on lower-mass or solar-type stars (Jouve et al. 2015; Emeriau-Viard & Brun 2017; Gouhier et al. 2021), while recent studies have begun to explore how multidimensional magneto-convective simulations can inform one-dimensional prescriptions for massive stars (Shimada et al. 2026).

The models analysed here are the first 3D MHD pre-supernova progenitors of this kind, including both the iron core and the surrounding burning shells. Their global properties, numerical setup, hydrostatic initialisation, turbulent shell structure, and nuclear-burning behaviour are presented in Paper I. Here we focus on the rotational and magnetic properties of the same models. We examine how the AM distribution evolves in convective and radiative regions, how magnetic fields are amplified in shells where SE models predict no fields, and how the final magnetic topology differs between radiative and turbulent layers.

This paper is structured as follows. Section 2 summarises the magnetic and rotation history of the progenitor models and describes how we initialise multidimensional models from the one-dimensional SE information. Section 3 presents the evolution of AM, magnetic-field amplification, and magnetic topology during the final pre-collapse phase. We then discuss in Section 4 the implications of our models and how they may be used to improve rotation and magnetic modelling in pre-supernova progenitors. Finally, Section 5 summarises our main conclusions.

2. Rotational and magnetic initial conditions

The SE progenitors and the multidimensional numerical setup are described in detail in Paper I. We consider two compact Wolf–Rayet-like progenitors. The first, G20, is a $20 M_{\odot}$ model computed with the version of GENEC presented in Griffiths et al. (2025). The second, M13, is taken from series B of Aguilera-Dena et al. (2020), computed with MESA. In the present paper we summarise only the aspects of the one-dimensional models that are directly relevant for the rotational and magnetic-field structure of the subsequent 3D MHD simulations.

2.1. Rotational and magnetic properties of 1D models

Models G20 and M13 are both fast rotators at birth, with initial surface rotation rates equal to 460 km s^{-1} and 600 km s^{-1} respectively. Transport of AM is induced through the TS-dynamo during SE. For model G20, the magnetic transport follows the prescription of Eggenberger et al. (2022) whereas M13 uses the description of Heger et al. (2005)—the two only differ by a calibration factor included in Eggenberger et al. (2022).

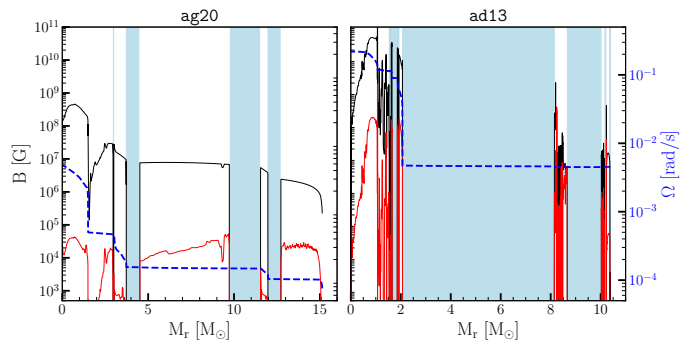


Fig. 1: Saturation field strengths at mapping for the toroidal component (black) and poloidal component (red) associated with the magnetic instabilities considered in model G20 (left) and M13 (right). The light blue bands indicate convective regions, where 1D SE models do not provide magnetic-field estimates. The blue dashed line shows the rotational frequency Ω .

The fast initial rotation combined with the strong coupling of rotation induced by magnetic torques results in a large amount of mass and AM loss driven by the fast velocities at the surface of each star. These winds result in the loss of the hydrogen envelope of both stars.¹

Table 1 summarises the total mass, total AM, and surface rotation rates at key evolutionary phases. By the end of core-helium burning, model G20 retains only a total AM of $\approx 10^{50} \text{ g cm}^2 \text{ s}^{-1}$, compared to $\approx 5 \times 10^{51} \text{ g cm}^2 \text{ s}^{-1}$ for model M13. These values correspond to approximately 1% and 25%, respectively, of their total AM at terminal age main sequence (TAMS). In both models, the greatest AM loss occurs after the TAMS, but this loss is much larger for G20. Thus, although the two progenitors have broadly similar compact pre-collapse structures (see Fig. 1 of Paper I), they differ strongly in their rotational content: M13 is much faster rotating than G20 both at the surface and in the core at the time of mapping to 3D.

The magnetic-transport prescriptions provide estimates of the saturated magnetic-field strengths in radiative regions, the exact expressions are given in Appendix A. Figure 1 shows the toroidal and poloidal saturation-field strengths used to initialise the 3D MHD-models. Convective regions are highlighted in light blue; in the one-dimensional SE models, these regions are not assigned initial magnetic-field strengths.

The field strengths obtained from these prescriptions should be regarded as order-of-magnitude estimates. In some layers, the magnetic energy implied by the saturation formulae, $E_B \sim \int_{\text{Shell}} \frac{1}{2} B^2 dV$, can become comparable to, or even exceed, the local rotational energy $E_{\Omega} \sim \int_{\text{Shell}} \frac{1}{2} \rho (r \sin \theta \Omega)^2 dV$, where B and Ω are the local magnetic field strength and rotational frequency, respectively. This would be unphysical if interpreted literally, since the magnetic energy ultimately derives from differential rotation. In such cases, a back-reaction should limit further field amplification. To prevent this situation in the initial conditions, we cap the toroidal saturation field so that the local ratio of magnetic to rotational energy does not exceed 0.1.

¹ Both models end as compact, hydrogen-poor progenitors. However, the origin of this structure differs between them: while G20 is stripped of its hydrogen-rich envelope, M13 becomes hydrogen- and helium-depleted through quasi-chemically homogeneous evolution, where rotational mixing and nuclear burning act together with rotationally enhanced mass loss.

Table 1: Total mass, total AM, and surface rotation of the progenitor models at different evolutionary phases. We define the TAMS as the point where central hydrogen mass fraction drops below 10^{-5} . Helium depletion is operatively defined as the time when the central helium mass fraction drops below 10^{-5} . The “final model” denotes the last model computed in the SE calculation.

	ZAMS		TAMS		He depletion		Final model	
	G20	M13	G20	M13	G20	M13	G20	M13
$M_{\text{tot}} [M_{\odot}]$	19.99	12.99	17.41	12.47	15.19	10.92	15.15	10.37
$L_{\text{tot}} [10^{52} \text{ g cm}^2 \text{ s}^{-1}]$	4.74	2.85	1.33	2.00	0.0118	0.516	0.0113	0.243
$\Omega_{\text{surf}} [10^{-4} \text{ rad s}^{-1}]$	1.30	2.31	1.58	4.38	0.192	18.2	0.942	43.8

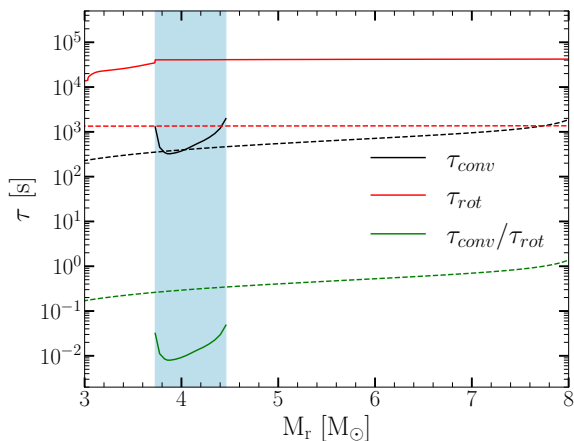


Fig. 2: Comparison of the convective turnover time τ_{conv} (black), rotational timescale τ_{rot} (red), and their ratio (green) for models G20 (solid) and M13 (dashed) at the mapping point. The blue-shaded region marks the oxygen convective shell of G20; the plotted range lies fully inside the broader oxygen convective shell of M13.

The peak field strengths in G20 are at least two orders of magnitude lower than in M13 (Fig. 1), primarily because of the much slower core rotation in G20. The estimated poloidal field is likewise weaker in G20, only reaching 10^5 G, whereas it peaks at $\sim 10^8$ G in the core of M13. If the 1D magnetic structure were taken at face value, the magnetised core would be separated from the outer magnetised layers by convective shells with no prescribed magnetic field (blue regions in Fig. 1). One of the central results of the present paper is that the 3D MHD evolution alters this picture: magnetic flux is transported into convective regions and amplified there, leading to magnetic connectivity across layers that are disconnected in the original SE estimate (Section 3).

The amplification of magnetic fields in stellar convective regions depends on the relative importance of convection and rotation. To assess this, we compare the corresponding convective turnover time and local rotational period,²

$$\tau_{\text{conv,SE}} = \frac{2H_p}{v_{\text{conv}}}, \quad (1)$$

where v_{conv} is the MLT estimate of the convective velocity and H_p is the pressure scale height. We estimate the rotational timescale with the local rotational period,

$$\tau_{\text{rot,SE}} = \frac{2\pi}{\Omega}. \quad (2)$$

² We denote these timescales with “SE” as they are computed using values from the SE models. This is in contrast with similar quantities that we will compute in later sections based on the 3D simulations.

The ratio of these two timescales is related to the Rossby number (see Varma & Müller 2023, for a similar, yet non-identical, definition) and measures whether rotation or convection dominates the local dynamics.

Figure 2 shows these timescales along with their ratio in the convective oxygen-burning shells for each progenitor (see the shaded regions of Fig. 1). In both models, the ratio is smaller than unity—i.e., convection is faster than rotation, as expected, since convection in advanced burning phases is extremely rapid and AM transport mediated by magnetic fields has substantially slowed the stellar cores. The ratio is roughly an order of magnitude larger in M13 than in G20, reflecting the much faster rotation of the MESA progenitor.

2.2. Initial magnetic-field and angular-momentum distributions.

The effective implementation of rotation and magnetic fields in 1D SE cannot specify their full 3D structure. Mapping such models into multidimensional MHD calculations therefore requires assumptions about both the angular-velocity distribution and the magnetic-field topology.

In 1D SE, rotation is usually assumed to be shellular, $\Omega = \Omega(r)$. This approximation is motivated by efficient horizontal transport along isobars, which tends to homogenise the rotational frequency on spherical shells during most evolutionary phases (e.g. Maeder & Meynet 2003). Near core collapse, however, the relevant dynamical and convective timescales become short, and the rotation profile need not remain shellular. An alternative limiting case is cylindrical rotation, in which Ω is constant on coaxial cylinders, i.e., $\Omega = \Omega(\varpi)$, where $\varpi = r \sin \theta$ is the distance to the rotational axis.

In the deep stellar interior, as the core approaches collapse, the true rotational structure likely lies between these two idealised limits and may vary between radiative and convective regions. Multidimensional simulations of rotating stars indeed show a reorganisation of rotation towards cylindrical isosurfaces within the envelope (Charbonneau & MacGregor 1993; Browning et al. 2004). In radiative zones, the preferred differential-rotation structure can also depend on the Prandtl number³ (Gouhier et al. 2021).

To assess the rotational profile in our progenitors, we performed a two-dimensional test simulation of model M13. Figure 3 compares the initial shellular angular-velocity distribution (left) with the state after 400 s of evolution (centre). The model rapidly develops a more cylindrical organisation outside the inner core, while the central region ($r \leq 10^8$ cm) remains closer to shellular rotation. To reduce the initial transient associated with this readjustment, the 3D models are initialised with

³ This is the ratio of kinematic viscosity to thermal diffusivity, which is generally very low in stellar interiors ($\sim 10^{-6}$).

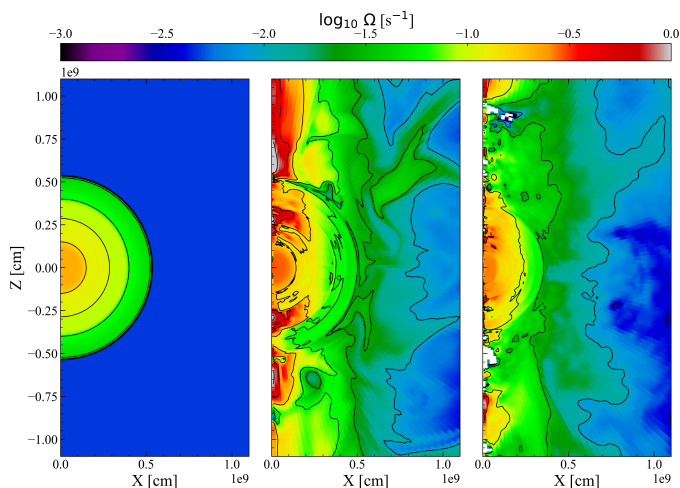


Fig. 3: Two-dimensional maps of the rotational frequency for the initial setup of a 2D test with shellular rotation (left), the resulting profile after 400 s of evolution (centre), and the ϕ -averaged 3D profile after 400 s of total evolution (right), obtained from a model initialised with the cylindrically weighted rotation profile described in the text. Black lines indicate iso-contours of Ω .

a cylindrically weighted angular-velocity distribution ($\Omega(r, \theta) = \Omega_{\text{SE}}(r)/(\sin \theta)$) rather than with a purely shellular one.⁴

This choice of initial setup was motivated by the 2D axisymmetric test. To check whether this cylindrical-like organisation is preserved during the subsequent 3D evolution, the right panel of Fig. 3 shows the ϕ -averaged angular-velocity map of the 3D model at $t = 400$ s, starting from the cylindrically weighted initial rotation profile. The resulting profile still shows a clear departure from shellular rotation, indicating that the cylindrical-like structure is not erased by the fully 3D turbulent evolution.

The magnetic-field strength can be estimated from the 1D SE prescriptions in radiative regions, but the field geometry is not specified. We therefore construct an initial axisymmetric field using the SE toroidal and poloidal saturation strengths. The toroidal component is assigned as

$$B_{\text{tor}}(r, \theta, \phi) = b_{\text{tor}}(r), \quad (3)$$

where b_{tor} is the SE toroidal saturation field (see Appendix A). The radial component is written as

$$B_r(r, \theta, \phi) = b_{\text{pol}}(r) \cos(n\theta), \quad (4)$$

where b_{pol} is the SE poloidal saturation field and we set $n = 1$ to generate a dipolar structure in each radial shell. The polar component $B_\theta(r, \theta, \phi)$ is then obtained by imposing the solenoidal constraint

$$\nabla \cdot \mathbf{B} = 0 \quad (5)$$

thus ensuring that the constructed initial field is divergence-free.

Figure 4 shows the resulting initial field geometry for model G20. The background colour map gives the toroidal field strength, while the streamlines represent the poloidal field. White regions show where the SE model does not initially prescribe a magnetic field, namely convective layers.

⁴ In the implementation used here, the mapped rotational frequency is capped near the rotation axis to avoid unphysically large values. The precise mapping should be kept consistent with the simulation setup, so that outside the core the rotational frequency does not exceed the core rotational rate.

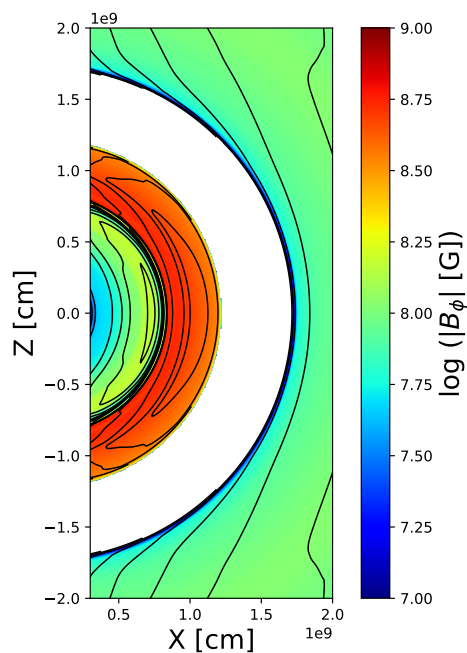


Fig. 4: Axial projection of initial poloidal magnetic-field lines for model G20. The background colour map shows the toroidal magnetic-field strength. The white region corresponds to layers where no magnetic field is prescribed by the 1D SE model.

3. Results

Using the setup outlined in Section 2 and in Paper I, we evolved both progenitors through the final minutes prior to collapse. Model G20 was evolved for 190 s in 3D, while model M13 was run for 320 s in 3D, after an initial 200 s of axisymmetric relaxation phase. As discussed in Paper I, these durations cover many convective turnovers in the inner burning shells, although the outer convective regions are less well sampled. The resulting models therefore provide a statistically robust description of the rotational and magnetic evolution in the inner convective regions, while the outer shells should be interpreted more cautiously.

The multidimensional evolution modifies both the AM distribution and the magnetic-field structure relative to 1D SE predictions in the convective regions. In the following, we first analyse the AM redistribution driven by hydrodynamic and magnetic stresses. We then examine magnetic-field amplification in radiative and convective regions, and finally characterise the topology of the magnetic field at the pre-SN link.

For reference, the region labels R1, C1, R2 and C2 follow the notation of Paper I: R1 denotes the radiative iron-core region, C1 the innermost turbulent shell, R2 the intervening radiative layer, and C2 the outer oxygen-burning convective shell. In model M13, C1 corresponds to a thin Si-burning shell, whereas in G20 it corresponds to the turbulent edge of the iron core.

3.1. Angular momentum evolution

We define the specific angular momentum about the rotation axis as $j = \Omega \varpi^2$, where $\varpi = r \sin \theta$ is the cylindrical radius. In radiative regions, the shell-averaged specific AM remains close to the initial SE value during the short pre-collapse interval considered here (Fig. 5). The radiative region R1 spins up as the star contracts, but its specific angular momentum is approximately con-

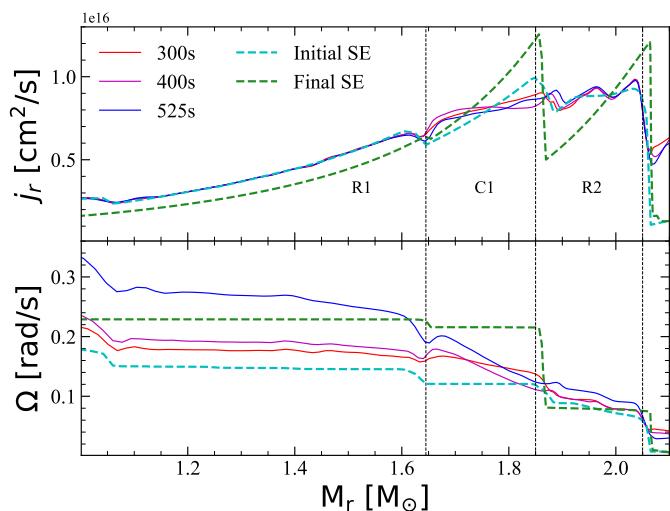


Fig. 5: Shell-averaged specific AM, top, and rotational frequency, bottom, for model M13 at different evolutionary times. The cyan and green lines show the corresponding SE profiles at mapping and at the pre-SN link, respectively. The figure focuses on the inner convective region C1 and its neighbouring radiative layers; the outer parts of the star are not shown.

served. The neighbouring radiative shell R2 shows small fluctuations in the multidimensional profiles, but its average evolution remains close to the SE prediction.

The main difference between the 3D MHD models and the SE predictions occurs in the convective region C1 (see the case of model M13 in Figure 5). In the SE model, this shell evolves toward nearly uniform rotational frequency. In the 3D model, by contrast, the shell develops substantial radial differential rotation: the base of the shell rotating faster than the top. Equivalently, the convective region evolves toward an approximately constant specific-angular-momentum profile. Since $j \approx \text{const.}$ implies $\Omega \propto \varpi^{-2}$, the resulting rotation profile differs markedly from the $\Omega \approx \text{const.}$ behaviour usually assumed for convective regions in 1D SE calculations.

A similar tendency is present in the convective regions of model G20, although it is harder to quantify there. Because G20 rotates much more slowly than M13, the azimuthal velocity associated with turbulent convective motions becomes comparable to, or even larger than, the mean rotational velocity in that model. For this reason, we occasionally observe negative values of local or shell-averaged Ω and j_r when convective motions dominate the azimuthal flow. This makes the interpretation of AM redistribution in G20 less clean than in the more rapidly rotating model M13.

In the outer convective shell C2 of M13, the same qualitative trend is visible: the base of the shell begins to spin up relative to the top. However, as shown in Paper I, this outer shell undergoes fewer convective turnovers during the 3D evolution. Its AM distribution has therefore not reached a quasi-stationary state as well defined as that of C1. We consequently focus the quantitative analysis below on the inner convective shell C1 of M13.

The tendency toward a constant- j_r is consistent with hydrodynamic simulations of Yoshida et al. (2021) and Varma & Müller (2023), where turbulent motions in convective shells redistribute angular momentum away from the $\Omega = \text{const.}$ state predicted by SE models. However, Varma & Müller (2023) found in their MHD model that magnetic stresses eventually

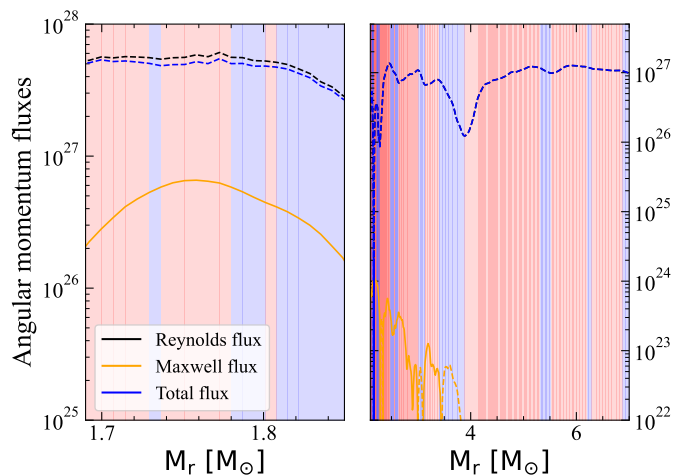


Fig. 6: Angular-momentum fluxes in the convective zones C1 (left) and C2 (right) of model M13. The Reynolds contribution is the sum of Eqs. (7)–(9), while the Maxwell contribution is given by Eq. (10). Solid lines represent positive fluxes and dashed lines negative fluxes. The background colouring is light red when $-\nabla_r F_{\text{tot}}$ in Eq. (6) is positive and blue when negative, corresponding to local increases or decreases in specific AM, respectively. In the right panel the blue and black dashed lines (i.e., the Reynolds and total fluxes) overlap.

counteracted the Reynolds stresses and restored a flatter angular-velocity profile. Since our models also develop magnetic fields in the convective regions it is necessary to determine why the same reversal does not occur here.

To analyse the AM transport, following Varma & Müller (2023), we write the radial part of the AM conservation equation⁵ as,

$$\frac{\partial \langle \rho v_{\phi} r \sin \theta \rangle}{\partial t} = -\nabla_r \cdot \langle \rho v_r v_{\phi} r \sin \theta - B_r B_{\phi} r \sin \theta \rangle, \quad (6)$$

where ∇_r denotes the radial term of the divergence and the angular brackets indicate a shell average. Applying the Reynolds and Favre decompositions (Favre 1965) defined in Appendix B, the radial AM flux can be decomposed into the following terms,

$$\text{Advective} : \langle \rho \tilde{v}_r (\tilde{\Omega} + \Omega'') r^2 \sin^2 \theta \rangle, \quad (7)$$

$$\text{Meridional} : \langle \rho v_r'' \tilde{\Omega} r^2 \sin^2 \theta \rangle, \quad (8)$$

$$\text{Turbulent} : \langle \rho v_r'' \Omega'' r^2 \sin^2 \theta \rangle, \quad (9)$$

$$\text{Magnetic} : -\langle B_r B_{\phi} r \sin \theta \rangle. \quad (10)$$

The first three terms are Reynolds fluxes, while the last term is the Maxwell flux.

Figure 6 shows the Reynolds flux, the Maxwell flux, and their sum for regions C1 and C2 of model M13. The fluxes are averaged over a time window of one convective turnover once the turbulent flow has reached a quasi-stationary state. The Maxwell flux has the opposite sign to the Reynolds flux. However, in region C1 its amplitude is roughly an order of magnitude smaller than that of the Reynolds flux at the peak. Magnetic stresses therefore do not dominate the angular-momentum transport in this shell.

⁵ Equation 14 in Varma & Müller (2023) contains typographical errors: the sign in front of the spatial derivative term ∇_r should be positive and the sign in front of the magnetic term negative. As we use Heaviside-Lorentz units, the 4π factor is not included in our definition.

The sign of $-\nabla_r F_{\text{tot}}$, where ∇_r is the radial component of the divergence operator, determines whether a given layer gains or loses AM. In C1 the left side of the shell is predominantly red in Fig. 6, indicating a local increase in AM, while the upper part of the shell is predominantly blue, indicating a local decrease. This is precisely the behaviour seen in Fig. 5: the base of the convective shell gains AM and spins up, while the upper part of the shell loses it. The net effect is a profile closer to constant j_r than to constant Ω .

The outer convective zone C2 shows a more fluctuating pattern. This is consistent with the fact that the region has not yet reached a quasi-stationary state. A longer simulation is required to determine whether C2 ultimately approaches the same constant- j_r configuration as C1, or whether magnetic stresses become more important once the turbulent state is fully established.

For progenitor M13, the Maxwell flux in C1 is too weak to counteract the hydrodynamic tendency toward a j_r -constant profile. Since the Maxwell stress scales with the product $B_r B_\phi$, an increase of both magnetic-field components by a factor of order a few would make the magnetic flux comparable to the Reynolds flux. In that case, the sign of the total flux divergence could reverse, allowing the shell to evolve back toward an Ω -constant profile.

The direction of AM transport in this convective region is finely balanced and only a small amount of amplification would reverse it. The magnetic field strengths in region C1 of M13 reach saturation strength, i.e. they will not grow further, so longer simulations are unlikely to change the distribution of AM we observe in the final model. Consequently, angular-momentum profiles of the stellar interior inferred directly from one-dimensional SE models may differ significantly from those obtained after a multidimensional MHD pre-collapse evolution.

3.2. Magnetic-field amplification

The magnetic field is amplified in all regions of both progenitors, but the dominant amplification mechanism differs between radiative and convective layers. In the radiative regions, the growth is modest and mainly associated with stellar contraction and the winding of the poloidal field into toroidal field by differential rotation. In convective regions, by contrast, turbulent motions transport magnetic flux from neighbouring magnetised layers and amplify both the poloidal and toroidal components. A cautionary note is warranted here. Owing to the limited resolution of 3D models, they may not fully capture the growth of the TS dynamo or the MRI, see Appendix C for further discussion. It is therefore quite possible that the magnetic-field amplification in the radiative regions of our models underestimates the true field growth in those layers. The field amplification reported here should therefore be interpreted as the result of the resolved multidimensional MHD evolution, supplemented by the numerical dissipation of the scheme, rather than as a complete description of all possible small-scale magnetic-instability growth in the stellar interior.

In the SE models, convective regions are assumed not to retain coherent magnetic fields after many turnover times, and therefore no magnetic field is prescribed in those regions (Fig. 1). Consequently, after mapping an SE model into a multidimensional MHD calculation, turbulent layers either remain initially unmagnetised, if they coincide with convective shells in the SE model, or contain only the field inherited from layers that are classified as radiative in the SE data but later become turbulent in the multidimensional evolution.

In model G20, region C1 develops turbulence in the multidimensional calculation even though it is not formally flagged as convective at the mapping time of the SE model, as discussed in Paper I. In that case, the SE model provides an initial magnetic field in region C1. We tested 2D models with and without this starting field in region C1 and found that the final field strength is controlled by the subsequent turbulent amplification rather than by the precise initial seed. In a statistical sense, quantified by the decomposition of the field in spherical harmonics (see Sect. 3.3), the field geometry was also independent of the initial choice as it was entirely driven by the turbulent motions occurring in the convective region. A similar situation occurs in C1 of M13, where non-zero SE magnetic-field estimates are present despite the layer being flagged as convective in SE.⁶ These tests indicate that, once turbulence develops, the final magnetic field in the convective shells is largely insensitive to the detailed seed field, provided that magnetic flux is available from the neighbouring radiative regions.

Figure 7 compares the angular-averaged poloidal and toroidal field strength at the beginning and end of the multi-D evolution. We point out the existence of two regions with no initial magnetic field as they are convective in the corresponding SE models. They are both located in the C2 regions, namely, from $\approx 2 M_\odot$ outward in model M13 and between $3.7 M_\odot$ and $4.2 M_\odot$ in model G20. During the 3D evolution magnetic flux is advected into these regions from the adjacent radiative layers and subsequently amplified by turbulent motions. As a result, regions that are magnetically disconnected in the 1D initial estimate become magnetically linked in the multidimensional models.

In the inner convective regions the initial poloidal and toroidal components increase by up to five orders of magnitude in some cases. By the end of the simulations, these regions have reached a quasi-saturated state in which the toroidal and poloidal components attain comparable strengths. The outer convective regions are not as close to reaching their asymptotic states, especially the upper part of C2 in M13, where the turbulent flow does not reach the entire oxygen shell before collapse.⁷ Nevertheless, the base of this shell reaches field strengths close to 10^9 G, even though the SE prescription initially assigns no magnetic field there.

Although some amplification of the poloidal field occurs in the radiative core and surrounding radiative shells, it generally remains weaker than the toroidal field. In the cores of both models, we observed only a modest increase in toroidal field strength, while the poloidal component is typically one to two orders of magnitude smaller.

The presence of magnetic fields in convective regions stands in stark contrast to the usual 1D SE treatment, in which magnetic fields are not prescribed in these layers. In classical flux-expulsion arguments, sustained convection can remove coherent magnetic flux from convective cells. Whether such expulsion operates efficiently in the present global 3D progenitor models is less clear. The effective magnetic Reynolds number in our simulations⁸ is of order 10^7 . Since the flux-expulsion timescale increases with R_m (Weiss 1966), the limited duration simulated

⁶ The origin of this inconsistency in the MESA model is unclear. Since the final field in the convective layers does not depend sensitively on the seed field, we initialise this layer with the SE field provided by the model.

⁷ See Paper I for discussions on the development of convection in that layer.

⁸ This is estimated using Fig.16 of Rembiasz et al. (2017) to obtain $\eta_{\text{mag}} \approx 10^8$ and then $R_m \sim \frac{v_{\text{conv}} H_p}{\eta_{\text{mag}}}$.

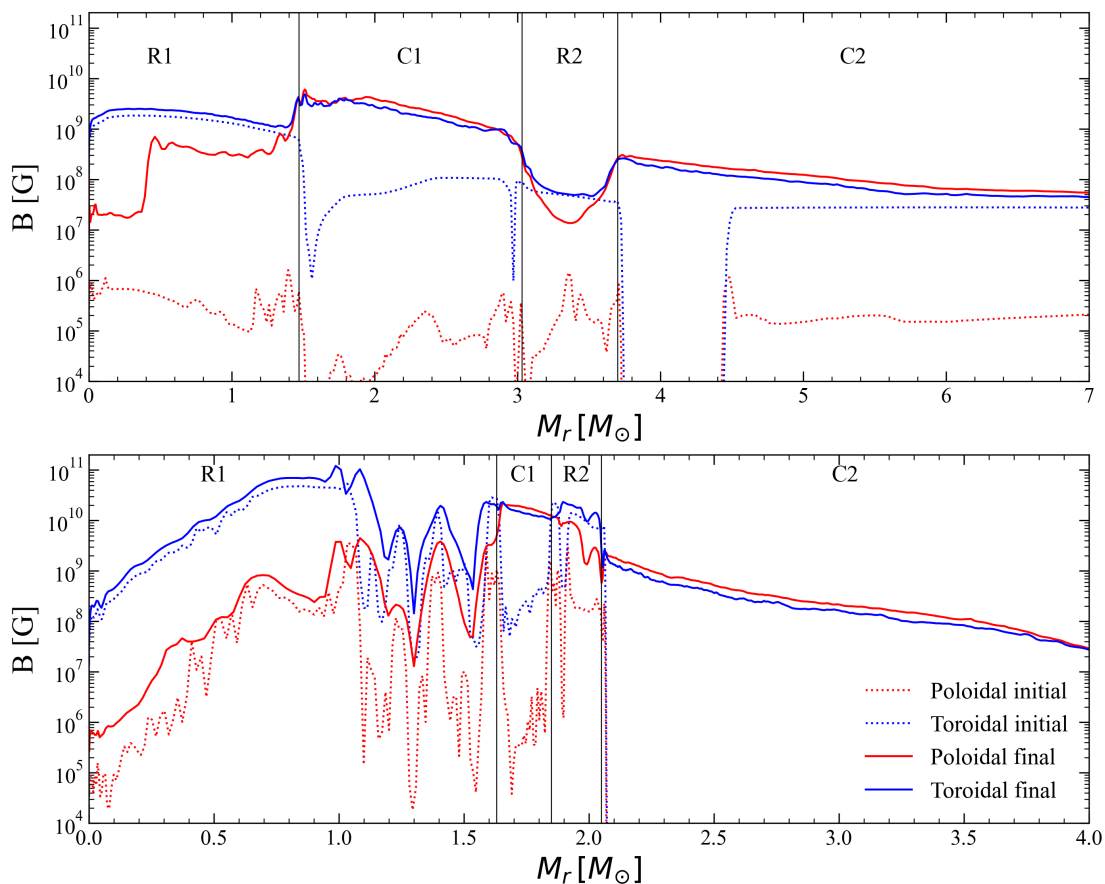


Fig. 7: Angular-averaged poloidal and toroidal magnetic fields at start (dotted lines) and end (solid lines) of multi-D evolution for models G20 (top) and M13 (bottom). The labels R and C denote radiative and convective regions, respectively, following the notation of Paper I.

prior to collapse may be insufficient for complete expulsion to occur. Moreover, the 3D turbulent flow continuously folds, stretches, and reconnects field lines through the effective numerical resistivity, providing additional pathways for maintaining magnetic flux in the convective layers.

A useful diagnostic of the magnetic-field structure is the winding length scale, defined as

$$\lambda = \frac{|\mathbf{B}|}{|\nabla \times \mathbf{B}|}. \quad (11)$$

In the inner convective shell C1 of M13, we find $\lambda/\Delta r \sim 1.5$, where Δr is the local grid size. Thus, the dominant winding scale remains resolved, although only marginally. As we do not explicitly include magnetic resistivity, dissipation occurs through the effective numerical resistivity of the scheme. Higher-resolution and longer-duration simulations would therefore be required to determine how robustly the small-scale magnetic structure survives and whether complete flux expulsion could occur on longer timescales.

Varma & Müller (2023) note that the magnitude of their saturated convective field is consistent, to within a factor of a few, with the saturation field strength expected from the MRI (Akiyama et al. 2003),

$$B_{\text{sat}}^2 \sim \rho r^2 \Omega^2 \left| \frac{d \ln \Omega}{d \ln r} \right|. \quad (12)$$

This estimate also provides a good description of the saturation strength in the convective regions in our models. For in-

stance, the saturation value predicted by Eq. 12 in C1 of M13 is 1.9×10^{10} G, whereas the average total field at the end of the simulation is 1.8×10^{10} G. However, as also pointed out by Varma & Müller (2023), this agreement should not be taken as evidence that the MRI is operating in the convective shell. Indeed, the MRI instability criterion,⁹ is generally not satisfied in the convective regions of the SE models. Rather, Eq. 12 provides a useful order-of-magnitude estimate for the saturation of a field amplified by radial differential rotation and turbulent shear (i.e., by magneto-shear).

To quantify more precisely the magnetic-field amplification, we use 4×10^6 Lagrangian tracer particles that follow and record their instantaneous velocity, magnetic-field strength, and position at each time step.¹⁰ Table 2 summarises the changes of the magnetic-field strength using tracer-averaged values within each region of interest.

In the radiative core, the toroidal-field amplification is mostly explained by contraction. For example, in R1 of M13 the tracer-averaged radii, \bar{r} decrease by a factor of $\bar{r}_{\text{ini}}/\bar{r}_{\text{fin}} \approx 1.86$. The square of this factor is 3.46, close to the measured toroidal-field factor estimated by the ratio $\bar{B}_{\text{tor,fin}}/\bar{B}_{\text{tor,ini}} \approx 3.75$ (Tab. 2), indicating that flux conservation accounts for most of the growth

⁹ See Eq. 6 of Griffiths et al. (2022)

¹⁰ For G20, tracer particles were activated at 128 s and therefore only record the final minute of the 3D evolution. The amplification factors reported in Table 2 for this model thus correspond to the interval from 128 s to collapse, not to the full simulation.

Table 2: Magnetic-field amplification measured using Lagrangian tracer particles in the 3D simulations. For each region, we report tracer-averaged quantities relevant to the magnetic-field evolution. A quantity denoted by \bar{X} corresponds to an average over tracers, while $\langle \cdot \rangle$ indicates an additional temporal average taken over a time interval during which the turbulent behaviour is approximately stationary.

Models	M13				G20			
	R1	C1	R2	C2	R1	C1	R2	C2
r_{\min} [10^8 cm]	0.2	2.8	4.1	5.5	0.5	2.5	9	12
r_{\max} [10^8 cm]	1.5	3.6	4.9	35	3.9	5.5	11	20
$B_{\max, \text{ini}}$ [10^{10} G]	15	5.3	5.6	0.14	4.9	6.1	1.3	0.077
$B_{\max, \text{fin}}$ [10^{10} G]	35	15	9.1	1.6	7.7	7.5	2.1	0.32
$\bar{r}_{\text{ini}}/\bar{r}_{\text{fin}}$	1.86	1.41	1.37	0.58	1.94	1.30	1.19	0.69
$\bar{B}_{\text{pol,fin}}/\bar{B}_{\text{pol,ini}}$	14.1	39	26.5	1200	4.99	2.99	3.02	4.66
$\bar{B}_{\text{tor,fin}}/\bar{B}_{\text{tor,ini}}$	3.75	21	2.45	18	6.31	12.2	4.38	10.3
$\langle \text{Ro}_f \rangle$	NA	8	NA	90	NA	195	NA	300
$\langle \bar{B}_{\text{tor}}/\bar{B}_{\text{pol}} \rangle$	47.6	0.877	4.55	0.741	7.69	0.746	3.03	0.741

in the radiative core. In contrast, the radiative shells R2 of both models exhibit toroidal-field growth larger than expected from contraction alone. This additional amplification reflects the exchange of magnetic flux with adjacent convective regions. An illustrative case is R2 of G20 (see Fig. 7), where the field at its boundaries grows until it approaches the strengths reached in the neighbouring convective zones, see Appendix D for more details.

The ratio between the toroidal and poloidal magnetic field strengths also differs between radiative and convective layers. Radiative regions remain toroidally dominated ($\langle \bar{B}_{\text{tor}}/\bar{B}_{\text{pol}} \rangle > 1$), whereas convective regions evolve toward approximate equipartition between the two components. Region C1 of M13 yields the closest ratio to 1, with the other convective regions seemingly converging towards $\sim 3/4$. This behaviour reflects the relatively rapid rotation in C1 of M13, which enhances the winding of turbulent poloidal field into toroidal field. This can be characterised by the fluid Rossby number,

$$\text{Ro}_f = \frac{|\omega|}{2\Omega}, \quad (13)$$

where $\omega = \nabla \times v$ is the local vorticity.¹¹ Therefore, for sufficiently high Rossby numbers, $\text{Ro}_f \gtrsim 90$, $\langle \bar{B}_{\text{tor}}/\bar{B}_{\text{pol}} \rangle$ converges towards $\sim 3/4$, i.e., to a slightly poloidally dominated configuration. Only in region C1 of M13, with a much lower Rossby number ($\text{Ro}_f \simeq 8$), does the ratio converge to a higher value. From the limited set of convective regions studied here we find a weak trend $\langle \bar{B}_{\text{tor}}/\bar{B}_{\text{pol}} \rangle \propto \text{Ro}_f^{-0.09}$. Given the small sample size, the limited numerical resolution, and the relatively large Rossby numbers of most regions, this scaling should be regarded as indicative rather than definitive. It nevertheless suggests that faster rotation favours a slightly more toroidally dominated saturated field, while slowly rotating convective shells approach a nearly balanced toroidal–poloidal configuration.

3.3. Magnetic field topology

By the time the progenitors reach the pre-SN link, their deep interiors are strongly magnetised. The resulting topology is, however, not uniform throughout the star. Radiative regions tend

¹¹ This definition follows Noraz et al. (2024) and generally leads to higher values than the definitions used in Varma & Müller (2023) and Shimada et al. (2026) for example.

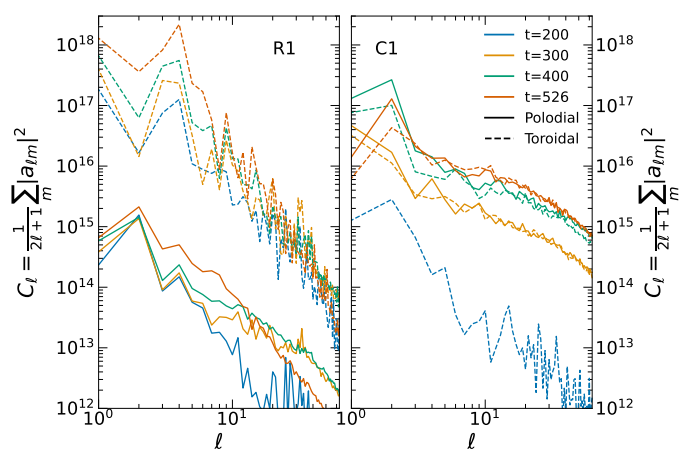


Fig. 8: Spherical-harmonic decomposition of the poloidal (solid lines) and toroidal (dashed lines) magnetic field components for model M13 in the radiative core R1 (left) and in the convective zone C1 (right).

to preserve a large-scale, predominantly toroidal field, whereas convective regions develop a more complex multiscale structure with substantial power at intermediate and high spherical-harmonic degrees.

To quantify this difference, we analyse the spherical-harmonic decomposition of the toroidal and poloidal magnetic-field components. For a scalar field $f(r, \theta, \phi)$, representing either the toroidal component, B_ϕ , or the poloidal field strength, $B_{\text{pol}} = (B_r^2 + B_\theta^2)^{1/2}$, we define

$$a_{\ell m}(r) = \int_{\Omega} f(r, \theta, \phi) Y_{\ell m}^*(\theta, \phi) d\Omega, \quad (14)$$

where $Y_{\ell m}$ are the complex spherical harmonics and

$$C_\ell(r) = \frac{1}{2\ell+1} \sum_{m=-\ell}^{m=\ell} |a_{\ell, m}|^2(r). \quad (15)$$

To reduce stochastic fluctuations and to track the same physical layers as the star contracts, the spectra are averaged over a small mass interval within each region of interest, rather than over a fixed radial interval.

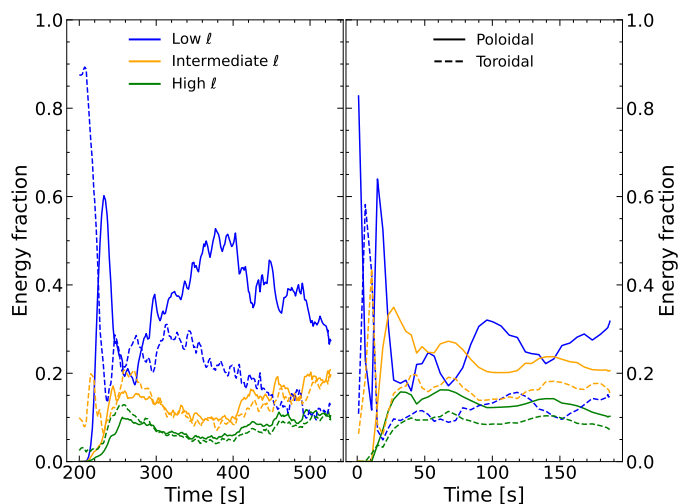


Fig. 9: Evolution of the normalised magnetic-energy distribution in the C1 zones of model M13 (left) and G20 (right). Poloidal contributions are shown with solid lines, and toroidal contributions with dashed lines, each normalised by the total magnetic energy. The energy is decomposed into three ranges of spherical harmonic degree: a low- ℓ range ($1 \leq \ell \leq 5$), an intermediate- ℓ range ($5 < \ell \leq 25$), and a high- ℓ range ($25 < \ell$).

Figure 8 shows the resulting spectra for model M13 in the radiative core R1 and in the inner convective shell C1. In the radiative core, the toroidal component dominates over the poloidal one. The poloidal-field spectrum peaks at $\ell = 2$, whereas the toroidal-field spectrum peaks over the range $\ell \simeq 1-4$. This large-scale structure remains broadly unchanged from the beginning of the 3D run—after 200 s of 2D evolution—to collapse. The main evolution observed in the spectra is in an overall increase in magnetic power, primarily at low multipoles, together with a modest transfer of power toward higher ℓ .

The convective region C1 behaves very differently. The initial geometry, inherited from the axisymmetric setup after the 2D relaxation phase, is rapidly reshaped once the fully 3D turbulent evolution begins. Between $t = 200$ s and $t = 300$ s, the poloidal and toroidal components both undergo substantial amplification and reach comparable power. The resulting spectrum is flatter than in the radiative core, with a peak at $\ell = 2$ for both components, and contains significant power over a wide range of ℓ . This reflects the stretching, folding, and reorientation of field lines by turbulent convection. Similar behaviour is found in the other convective regions of our models. The contrast between R1 and C1 therefore shows that the final magnetic topology is not well represented by a single large-scale dipolar or toroidal component throughout the star.

To follow the redistribution of magnetic power in time, we group the magnetic energy into three spherical-harmonic ranges: low ℓ , with $1 \leq \ell \leq 5$; intermediate ℓ , with $5 < \ell \leq 25$; and high ℓ , with $25 < \ell$. These ranges are not meant to define physically sharp regimes, but they provide a useful diagnostic of the transfer of magnetic energy from large-scale to smaller-scale structures.

Figure 9 shows this decomposition for the C1 regions of both 3D models. In both progenitors, most of the magnetic power initially resides at low ℓ , reflecting the large-scale field imposed in the initial conditions and preserved during the preceding 2D relaxation phase. Once the 3D turbulent evolution begins, a significant portion of the magnetic energy rapidly shifts to the intermediate- and high- ℓ ranges. In model M13, the high- ℓ contri-

bution eventually dominates, with the poloidal and toroidal components each contributing close to 30% of the total magnetic energy. In model G20, the low- ℓ modes remain the largest single contribution, but the power in these modes is strongly reduced compared to its initial value, and the intermediate- and high- ℓ ranges acquire a significant fraction of the total power.

This redistribution is largely confined to convective layers. In radiative regions, not shown in Fig. 9, over 90% of the magnetic energy remains in low- ℓ modes throughout the evolution. The final progenitors therefore contain two distinct types of magnetic topology: large-scale, predominantly toroidal fields in radiative regions, and multi-scale, approximately toroidal–poloidal fields in convective shells. A complementary visualisation of this structure is shown in Appendix E.

4. Discussion

The models presented here show that multidimensional MHD evolution can substantially modify the rotational and magnetic structure inherited from one-dimensional SE calculations during the final minutes before core collapse. Two results are particularly relevant. First, angular-momentum transport in convective regions does not necessarily preserve the nearly rigid rotation predicted by one-dimensional SE models; in our simulations, Reynolds stresses drive the flow toward an approximately constant specific-angular-momentum profile, while Maxwell stresses oppose this tendency but do not dominate it. Second, convective shells that are initially unmagnetised in the SE prescription become magnetised through flux transport from neighbouring radiative layers and subsequent turbulent amplification.

These results do not yet define a universal prescription. They are based on two progenitors and on a limited number of convective shells, with the outer shells less well sampled than the inner ones. Nevertheless, they provide useful guidance for constructing more realistic core-collapse initial conditions and for improving the treatment of magneto-convective angular-momentum transport in 1D SE.

4.1. Implications for core-collapse initial conditions

The 3D progenitors constructed here are intended for future collapse and explosion calculations. However, producing fully multidimensional pre-collapse models for a broad grid of stellar masses, metallicities, rotation rates, and magnetic-transport prescriptions is not computationally feasible. A practical alternative is to use multidimensional calculations such as these to guide the construction of improved initial conditions from 1D SE models.

The first implication concerns the angular-velocity distribution. Stellar-evolution models usually assume shellular rotation, $\Omega = \Omega(r)$. Our two-dimensional test calculation, however, shows that the rotation profile can reorganise toward a more cylindrical structure during the final pre-collapse evolution. The ϕ -averaged 3D profile shown in Fig. 3 further shows that this cylindrical-like organisation is not erased by the subsequent fully 3D turbulent evolution. Moreover, within convective regions the 3D simulations tend to develop approximately constant- j profiles rather than the nearly constant- Ω profiles predicted by SE. Mapping a 1D progenitor directly into a core-collapse calculation with a purely shellular rotation law may therefore misrepresent the angular-momentum distribution in the material that later accretes onto the proto-neutron star.

Rotation laws approaching constant specific angular momentum at large cylindrical radius have been used previously

in idealised magnetorotational core-collapse simulations. A standard example is the classical “ j -constant” law, $\Omega(\varpi) = \Omega_0/(1 + (\varpi/A)^2)$ (where A is a constant; [Eriguchi & Mueller 1985](#); [Obergaullinger et al. 2006b,a](#)). More recent magnetorotational core-collapse simulations often impose other parametric differential-rotation profiles (e.g. [Takiwaki et al. 2004](#); [Kuroda et al. 2020](#); [Shankar et al. 2026](#)).

The AM distribution in the pre-SN model is especially relevant for magnetorotational explosions. It controls the centrifugal support of the collapsing core, the winding of magnetic field lines, the rotational energy available to the proto-neutron star, and the conditions for jet formation. A cylindrical or constant- j redistribution changes where angular momentum is concentrated relative to the rotation axis and to the mass shells that accrete earliest. The quantitative impact of this redistribution must be assessed with collapse simulations, but the present results suggest that the rotational mapping from SE models should not be treated as a purely technical choice.

The second implication concerns the magnetic field. In standard SE models, magnetic-field estimates are typically available only in radiative regions, while convective shells are often assigned no field. Our simulations show that this can produce an artificially disconnected initial magnetic structure. In the multidimensional evolution, magnetic flux is transported into convective shells and amplified there until the toroidal and poloidal components reach comparable strengths. Thus, collapse calculations initialised directly from SE models should not necessarily leave convective regions unmagnetised.

A possible practical approach is the following. In radiative regions one may use the saturation-field estimates provided by the SE magnetic-transport prescription, while keeping in mind their order-of-magnitude nature. In convective regions, one may initialise a non-zero magnetic field using a shear-based saturation estimate such as Eq. 12 as an order-of-magnitude estimate of the field strength reached by turbulent shear amplification. The relative toroidal and poloidal components could then be chosen close to equipartition, as suggested by the convective regions in our models. For slowly rotating convective shells, our simulations indicate $\langle \bar{B}_{\text{tor}}/\bar{B}_{\text{pol}} \rangle \simeq 0.7 - 0.8$, while the more rapidly rotating C1 shell of M13 approaches a ratio closer to unity.¹² To test the robustness of this scaling, it will be necessary to examine additional progenitors with burning shells spanning a wider range of Rossby numbers, including values closer to, or even below unity. Achieving such conditions may be difficult during late burning stages. In SE models evolved with magnetic-field-driven AM transport, the core is significantly spun down compared with hydrodynamic models, while convection during silicon and oxygen shell burning remains very rapid. One possible avenue to reach lower Rossby numbers is through binary mergers, which can produce rapidly rotating cores even when magnetic AM transport is active. Such systems might yield turbulent shells with lower Rossby numbers and, perhaps, correspondingly weaker poloidal fields relative to toroidal fields.

The topology of the reconstructed field is also expected to be important for the post-bounce dynamics. Radiative regions in our models preserve most of their magnetic energy at low spherical-harmonic degree, whereas convective regions develop substantial power at intermediate and high ℓ . The present spectra suggest that low-order poloidal components, in particular $\ell = 2$, may be important. However, higher-resolution simulations that better capture small-scale instability growth may modify this con-

clusion. In the convective regions, the field contains much more power on small scales. Therefore, the final power spectra of our 3D models may provide a useful guide for initialising generic fields in the convective regions of new progenitors.

Before discussing magnetic-flux survival during early accretion, it is useful to recall a structural result from [Paper I](#). In the original 1D model of M13, the Si- and O-burning shells merge before collapse, whereas the 3D MHD evolution preserves a distinct Si-burning C1 shell separated from the O-burning C2 shell by the radiative layer R2. The discussion of magnetic-flux survival below therefore refers to the multidimensional pre-collapse structure, not simply to the original 1D SE profile.

To assess the longevity of the magnetic field in convective regions, the comparison with [Gottlieb et al. \(2024\)](#) is particularly relevant for model M13, which is both compact and rapidly rotating. In this model, the radiative iron core is expected to form the initial proto-neutron star, while the first layers to accrete after bounce belong to the silicon-burning shell C1, the intervening radiative layer R2, and then the inner part of the oxygen-burning shell C2. This ordering matters for the interpretation of magnetic-flux survival. The argument of [Gottlieb et al. \(2024\)](#) is most directly applicable to magnetic fields generated locally by small-scale AM-transport instabilities in radiative layers, where short coherence lengths, incoherent polarity, and reconnection may strongly reduce the net large-scale flux delivered to the compact object. In M13, however, the radiative layer R2 between C1 and C2 occupies only a relatively narrow mass interval, whereas most of the material accreted once the proto-neutron star reaches $M \gtrsim 1.6 M_{\odot}$ comes from convective layers.

Our 3D pre-collapse evolution suggests that these convective layers should not be treated in the same way as radiative layers whose magnetic fields are generated locally by small-scale AM-transport instabilities. In C1 and in the inner part of C2, magnetic flux is transported from neighbouring radiative regions and then amplified and maintained by the resolved turbulent flow. Once the turbulent state is established, the magnetic-energy spectrum and the relative distribution of power over spherical-harmonic degree evolve only moderately before collapse. Thus, on the resolved scales of our simulations, the magnetic structure in the convective layers is not erased before the pre-SN link. Since these layers are expected to dominate the early post-bounce accretion after the initial core has formed the proto-neutron star, their magnetic field may provide a more robust contribution to the magnetic flux accreted by the compact object than would be inferred from a purely 1D radiative-instability picture.

This suggests that the pre-collapse magnetic structure relevant for early accretion may be less vulnerable to the flux-cancellation argument than a purely radiative, small-coherence-length field. This does not imply that the net large-scale flux reaching the proto-neutron star is guaranteed to be conserved: the convective fields are multiscale and locally incoherent, and the accreted flux will depend on how this structure is compressed, advected, reconnected, and wound during infall and post-bounce evolution. In compact rapidly rotating progenitors like M13, a significant fraction of the early accreted mass is magnetised by convective turbulent amplification before collapse, and this field survives until the pre-SN link in the present 3D MHD simulations. Whether this flux contributes coherently to the proto-neutron star field can only be assessed with collapse simulations initialised from the present 3D models.

¹² The weak Rossby-number trend found in Section 3.2 should be regarded as indicative rather than as a calibrated scaling.

4.2. Implications for stellar-evolution modelling

The presence of magnetic fields in convective regions also has implications for 1D SE calculations. In SE models, convection is usually assumed to redistribute angular momentum toward nearly uniform angular velocity. In our 3D simulations, hydrodynamic Reynolds stresses instead drive the convective flow toward an approximately constant- j profile. Magnetic stresses act in the opposite direction and tend to restore a flatter Ω profile, but in our models they are not strong enough to overcome the Reynolds stresses.

Our results differ from the MHD model of [Varma & Müller \(2023\)](#), where Maxwell stresses developed in the convective regions become strong enough to reverse the hydrodynamic AM flux and restore a more rigidly rotating convective shell. The difference is not necessarily contradictory. The sign and magnitude of the net AM transport depend sensitively on the strength of the saturated magnetic field and on the correlation between the radial and toroidal field components, B_r, B_ϕ . In our C1 shell of M13, increasing both magnetic-field components by a factor of only a few would make the Maxwell flux comparable to the Reynolds flux and could reverse the direction of the net transport.

Several factors may therefore affect the final AM profile. One is the magnetic-field strength at the boundaries of the convective region. In simulations that excise part of the star, imposed magnetic boundary conditions may influence the field amplification inside the convective shell. [Varma & Müller \(2023\)](#) set a fixed vertical-field of 10^7 G at their inner radial boundary. In our global models, the field is evolved self-consistently, and neighbouring radiative layers exchange magnetic flux with the turbulent shells. In [Appendix D](#) we show the evolution of the poloidal and toroidal magnetic fields at selected boundaries of our convective regions.

A second factor is numerical resolution. The saturated field strength in turbulent MHD simulations can depend on the effective magnetic Reynolds number and on the numerical diffusivity of the scheme (e.g., [Varma & Müller 2026](#)). This is particularly relevant when the Maxwell stress is close to the threshold required to reverse the AM flux. Higher-resolution calculations, or calculations with controlled explicit diffusivities, would be needed to determine whether the saturation field in the present models is slightly underestimated. In this context, numerical diffusivity studies such as [Rembiasz et al. \(2017\)](#) are directly relevant for assessing the reliability of magnetic-field amplification in global MHD simulations.

The broader implication is that AM transport in convective shells should not be prescribed solely as a tendency towards rigid rotation. Instead, it may depend on the balance between hydrodynamic Reynolds stresses, which favour constant- j profiles, and Maxwell stresses, which can favour flatter Ω profiles if the magnetic field becomes sufficiently strong. Recent work by [Shimada et al. \(2026\)](#) points in this direction by relating Maxwell stresses in magneto-convective regions to local rotational and convective properties of the star. Our results support the need for such prescriptions, but also show that the field strength, topology, and boundary exchange of magnetic flux can be decisive.

4.3. Possible impact on collapse and explosion

The impact of these multidimensional progenitors on the subsequent collapse and explosion remains to be quantified by dedicated core-collapse simulations. Nevertheless, the differences found here identify several channels through which the outcome

may change relative to calculations initialised from the original one-dimensional SE models.

The first is the spin-up of the proto-neutron star. In model M13, the inner convective shell C1 evolves toward a constant- j profile, so the angular momentum contained in the lower part of the shell differs from the SE prediction. If a significant fraction of this shell accretes onto the proto-neutron star, the resulting spin-up can differ from that obtained from the 1D progenitor. This may affect the rotational energy available after bounce and the degree of differential rotation that can wind magnetic fields.

The second is the magnetic topology accreted by the collapsing core. In the original SE magnetic-field estimate, the magnetised core and overlying magnetised layers are separated by convective regions where no field is prescribed. In the 3D models, these regions become magnetically connected. Convective shells also develop a substantial poloidal component and a multiscale, tangled topology. During collapse, such a field may be compressed, stretched, and wound into a different configuration from that obtained by collapsing a simple dipolar or toroidal field ([Aloy & Obergaulinger 2021](#); [Obergaulinger & Aloy 2021](#)).

The third is the magnetic field available for jet launching or collimation. Radiative regions retain a large-scale, predominantly toroidal structure, whereas convective regions contain a broader distribution of multipoles. Large-scale components may be more effective in organising an outflow ([Bugli et al. 2021](#)), while the role of small-scale components is not obvious (they may partly cancel or reconnect during infall). The balance between these effects will depend on how much of the convective-shell topology survives collapse and how it is processed by the proto-neutron star and post-shock flow.

5. Conclusions

We have analysed the rotational and magnetic properties of the first full 3D MHD pre-supernova progenitors evolved through the final minutes before core collapse. The global properties, turbulent shell structure, and nuclear-burning behaviour of these models were presented in [Paper I](#); here we have focused on angular momentum redistribution, magnetic-field amplification, and magnetic topology.

Our main results can be summarised as follows. First, the AM distribution obtained from the multidimensional evolution can differ substantially from the 1D SE. In the inner convective shell of model M13, Reynolds stresses drive the flow toward an approximately constant specific-angular-momentum profile, corresponding to an average rotation profile close to $\Omega \propto \varpi^{-2}$. Maxwell stresses oppose this tendency, but in our models they are not strong enough to restore the nearly rigid rotation usually assumed for convective regions in 1D SE calculations. The final pre-collapse rotation profile is therefore sensitive to the balance between hydrodynamic and magnetic stresses.

Second, convective regions that are initially weakly magnetised, or even unmagnetised in the 1D SE prescription, acquire and amplify magnetic flux during the 3D evolution. Magnetic flux is transported from neighbouring radiative regions into the turbulent shells, where both the poloidal and toroidal components are amplified. In the convective regions, the saturated field approaches approximate toroidal–poloidal equipartition, with $B_{\text{tor}}/B_{\text{pol}} \approx 0.7\text{--}0.8$ in slowly rotating shells and a ratio closer to unity in the faster rotating C1 shell of M13.

Third, the magnetic topology differs markedly between radiative and convective layers. Radiative regions largely preserve a low- ℓ , predominantly toroidal magnetic structure, whereas convective regions develop a multiscale field with substantial

power at intermediate and high spherical-harmonic degrees. Thus, the pre-collapse field cannot be represented accurately by a single large-scale dipolar or toroidal component throughout the star. A more realistic construction of magnetic initial conditions for collapse simulations should account for both large-scale fields in radiative layers and turbulent, multiscale fields in convective shells.

Finally, our results suggest that multidimensional pre-collapse evolution can modify the magnetic connectivity of the progenitor. Regions that are magnetically disconnected in the 1D SE estimate become linked through flux transport and turbulent amplification. This may affect the magnetic flux and topology accreted by the proto-neutron star, the subsequent winding of field lines, and the conditions for magnetorotational outflows. Quantifying these effects requires collapse and post-bounce simulations initialised from the present 3D progenitors. Nevertheless, the models presented here already show that AM and magnetic-field structures inferred directly from 1D SE calculations may be incomplete, especially in the convective shells that accrete shortly after bounce.

6. Data Availability

The final 3D snapshots at the pre-SN link of each progenitor are stored on Zenodo <https://doi.org/10.5281/zenodo.19692957>. They will be made publicly available from 01/01/2027. For anticipated access please contact the corresponding author.

Acknowledgements. We acknowledge support from grants PID2021-127495NB-I00 and PID2025-171322NB-C22, funded by MCIN/AEI/10.13039/501100011033 and by the European Union “NextGenerationEU”. We also acknowledge support from the Astrophysics and High Energy Physics programme of the Generalitat Valenciana ASFAE/2022/026 funded by MCIN and the European Union NextGenerationEU (PRTR-C17.I1) as well as support from the Prometeo excellence programme grant CIPROM/2022/13 funded by the Generalitat Valenciana.

References

- Aguilera-Dena, D. R., Langer, N., Antoniadis, J., & Müller, B. 2020, *The Astrophysical Journal*, 901, 114
- Akiyama, S., Wheeler, J. C., Meier, D. L., & Lichtenstadt, I. 2003, *The Astrophysical Journal*, 584, 954–970
- Aloy, M. Á. & Obergaulinger, M. 2021, *Monthly Notices of the Royal Astronomical Society*, 500, 4365–4397
- Balbus, S. A. & Hawley, J. F. 1991, *The Astrophysical Journal*, 376, 214
- Browning, M. K., Brun, A. S., & Toomre, J. 2004, *The Astrophysical Journal*, 601, 512–529
- Bugli, M., Guilet, J., & Obergaulinger, M. 2021, *Monthly Notices of the Royal Astronomical Society*, 507, 443–454
- Burrows, A., Dessart, L., Livne, E., Ott, C. D., & Murphy, J. 2007, *ApJ*, 664, 416
- Charbonneau, P. & MacGregor, K. B. 1993, *The Astrophysical Journal*, 417, 762
- Eggenberger, P., Moyano, F. D., & Den Hartogh, J. W. 2022, *Astronomy and Astrophysics*, 664, L16
- Emeriau-Viard, C. & Brun, A. S. 2017, *The Astrophysical Journal*, 846, 8
- Eriguchi, Y. & Mueller, E. 1985, *A&A*, 146, 260
- Favre, A. J. 1965, *Journal of Applied Mechanics*, 32, 241
- Gottlieb, O., Renzo, M., Metzger, B. D., Goldberg, J. A., & Cantiello, M. 2024, *ApJ*, 976, L13
- Gouhier, B., Lignières, F., & Jouve, L. 2021, *Astronomy & Astrophysics*, 648, A109
- Griffiths, A., Aloy, M.-A., Hirschi, R., et al. 2025, *Astronomy and Astrophysics*, 693, A93
- Griffiths, A., Aloy, M.-Á., & Obergaulinger, M. 2026a, *Astronomy & Astrophysics*, submitted [Paper I]
- Griffiths, A., Aloy, M.-Á., & Obergaulinger, M. 2026b, *Astronomy & Astrophysics*, submitted [Paper II]
- Griffiths, A., Eggenberger, P., Meynet, G., Moyano, F., & Aloy, M.-Á. 2022, *Astronomy and Astrophysics*, 665, A147
- Heger, A., Woosley, S. E., & Spruit, H. C. 2005, *The Astrophysical Journal*, 626, 350
- Jouve, L., Gastine, T., & Lignières, F. 2015, *Astronomy & Astrophysics*, 575, A106
- Kuroda, T., Arcones, A., Takiwaki, T., & Kotake, K. 2020, *ApJ*, 896, 102
- Maeder, A. & Meynet, G. 2003, *Astronomy & Astrophysics*, 411, 543–552
- Müller, B. 2024, arXiv e-prints, arXiv:2403.18952
- Mösta, P., Richers, S., Ott, C. D., et al. 2014, *The Astrophysical Journal*, 785, L29
- Nomoto, K., Tanaka, M., Tominaga, N., Maeda, K., & Mazzali, P. A. 2007, *Hypernovae and their Gamma-Ray Bursts Connection*
- Noraz, Q., Brun, A. S., & Strugarek, A. 2024, *Astronomy & Astrophysics*, 684, A156
- Obergaulinger, M. & Aloy, M. Á. 2017, *MNRAS*, 469, L43
- Obergaulinger, M. & Aloy, M. Á. 2020, *Monthly Notices of the Royal Astronomical Society*, 492, 4613–4634
- Obergaulinger, M. & Aloy, M. Á. 2021, *Monthly Notices of the Royal Astronomical Society*, 503, 4942–4963
- Obergaulinger, M., Aloy, M. A., Dimmelmeier, H., & Müller, E. 2006a, *A&A*, 457, 209
- Obergaulinger, M., Aloy, M. A., & Müller, E. 2006b, *A&A*, 450, 1107
- Reichert, M., Bugli, M., Guilet, J., et al. 2024, *Monthly Notices of the Royal Astronomical Society*, 529, 3197–3209
- Reichert, M., Obergaulinger, M., Aloy, M. Á., et al. 2022, *Monthly Notices of the Royal Astronomical Society*
- Rembiasz, T., Guilet, J., Obergaulinger, M., et al. 2016, *Monthly Notices of the Royal Astronomical Society*, 460, 3316–3334
- Rembiasz, T., Obergaulinger, M., Cerdá-Durán, P., Aloy, M.-Á., & Müller, E. 2017, *ApJS*, 230, 18
- Shankar, S., Mösta, P., Haas, R., & Schnetter, E. 2026, *MNRAS*, 548, stag646
- Shimada, R., McNeill, L. O., Varma, V., et al. 2026, *The Astrophysical Journal*, 1002, 66
- Spruit, H. C. 2002, *Astronomy and Astrophysics*, 381, 923–932
- Takiwaki, T., Kotake, K., Nagataki, S., & Sato, K. 2004, *ApJ*, 616, 1086
- Varma, V. & Müller, B. 2021, *Monthly Notices of the Royal Astronomical Society*, 504, 636–647
- Varma, V. & Müller, B. 2023, *Monthly Notices of the Royal Astronomical Society*, Volume 526, Issue 4, pp.5249–5262, 526, 5249
- Varma, V. & Müller, B. 2026, *Monthly Notices of the Royal Astronomical Society*, 548, stag626
- Varma, V., Müller, B., & Schneider, F. R. N. 2023, *MNRAS*, 518, 3622–3636
- Weiss, N. O. 1966, *Proceedings of the Royal Society of London Series A*, 293, 310
- Woosley, S. E. & Bloom, J. S. 2006, *Annual Review of Astronomy and Astrophysics*, 44, 507–556
- Yoshida, T., Takiwaki, T., Kotake, K., et al. 2021, *ApJ*, 908, 44
- Zha, S., Müller, B., & Powell, J. 2024, *The Astrophysical Journal*, 969, 141

Appendix A: Field strengths

Magnetic instabilities are treated in stellar-evolution calculations through effective prescriptions. Their impact is on the diffusion of angular momentum and chemical species when appropriate. In G20 the description of the TS dynamo follows Eggenberger et al. (2022) which represents a calibrated description of the original formalism proposed by Spruit (2002). Model M13 describes the TS dynamo using the description of Heger et al. (2005).

In the case of the TS dynamo as described by Eggenberger et al. (2022) the saturation field expressions are¹³

$$b_{\text{tor}} = \sqrt{\rho} C_T |q| \Omega r \frac{\Omega}{N}, \quad (\text{A.1})$$

$$b_{\text{pol}} = \sqrt{\rho} C_T^2 q^2 \Omega r \left(\frac{\Omega}{N} \right)^3. \quad (\text{A.2})$$

Here $q = \frac{\partial \ln \Omega}{\partial \ln r}$ is the shear of the rotating flow, N the Brunt-Väisälä frequency and C_T a calibration factor set to 216. In the case of the Heger et al. (2005) description no such calibration factor is applied and the expressions are the same as above but with $C_T = 1$.

Appendix B: Reynolds and Favre decomposition

The Reynolds and Favre decompositions of a fluid quantity X are respectively given by

$$\hat{X} = \langle X \rangle = \frac{\int_{\omega} X d\omega}{\int_{\omega} d\omega} \quad (\text{B.1})$$

and

$$\tilde{X} = \frac{\int_{\omega} \rho X d\omega}{\int_{\omega} \rho d\omega} \quad (\text{B.2})$$

where $d\omega = \sin \theta d\theta d\phi$ is the solid angle element. *Fluctuating* variables are defined with respect to the Reynolds and Favre averages as

$$X' = X - \hat{X}, \quad X'' = X - \tilde{X}. \quad (\text{B.3})$$

Appendix C: Capturing the magnetorotational instability

Our 3D simulations show an amplification of magnetic field strength, particularly in convective regions where the saturated field strength follows a shear-based saturation estimate formally similar to the MRI saturation estimate. To resolve magnetic instabilities in our simulations we need sufficient spatial resolution to capture the fastest growing mode along with sufficient simulation time to clearly see the impact of the instability on the magnetic field.

For the MRI the fastest growing mode is roughly given by (Balbus & Hawley 1991),

$$\lambda_{\text{MRI}} = \frac{2\pi B}{\Omega \sqrt{\rho}}. \quad (\text{C.1})$$

¹³ Note that in the Heaviside-Lorentz units that we use here there is no factor $\sqrt{4\pi}$.

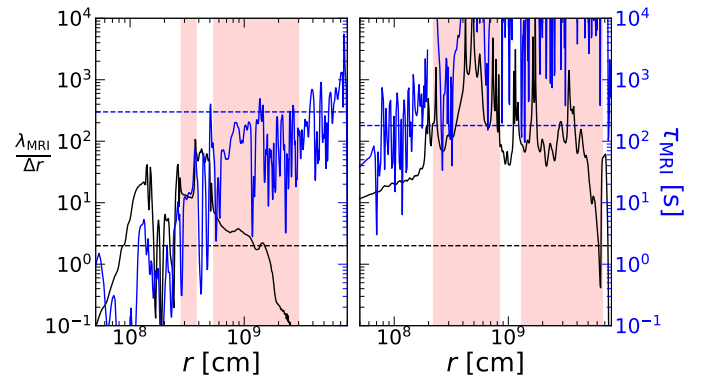


Fig. C.1: Ratio of the fastest growing mode, Eq. C.1, and the radial grid size in model M13 (left) and model G20 (right). The dashed black line indicates $\lambda_{\text{MRI}}/\Delta r = 2$. In blue we show both the growth timescale of the MRI, Eq. C.2, and the total 3D simulation time for each model (dashed horizontal line). The red zones delimit the convective regions for each model.

To capture MRI growth, the spatial resolution must be sufficient to resolve the fastest-growing mode, with at least two grid cells per wavelength, although larger quality factors are preferable. Capturing the nonlinear termination of the MRI by parasitic instabilities requires somewhat higher resolution, typically of order 2–4 times finer than the fastest-growing wavelength (see Rembiasz et al. 2016). Since the radial resolution of our grid is not uniform, Fig. C.1 shows the ratio between the fastest-growing MRI wavelength and the radial cell size as a function of radius. In model G20 (right panel), this ratio is well above 10 throughout the computational domain, owing to the slow rotation of the model, which leads to large values of λ_{MRI} . In model M13, the fastest-growing wavelength is much smaller. Nevertheless, according to this resolution criterion, the MRI is resolved throughout the convective zone C1, the radiative zone R2, and the base of C2.

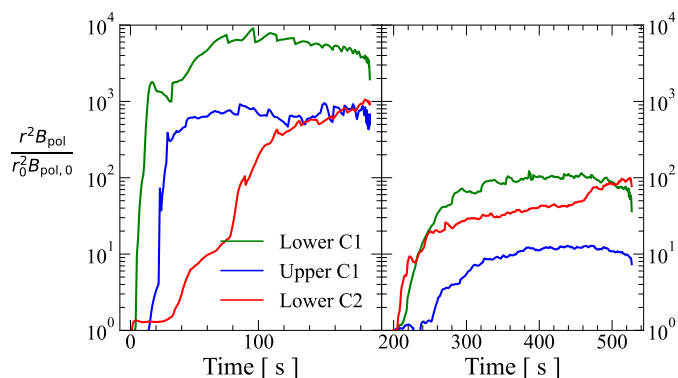
We further estimate the typical growth timescale of the MRI as,

$$\tau_{\text{MRI}} = \gamma_{\text{MRI}}^{-1} = \left(\frac{q}{2} \Omega \right)^{-1}, \quad (\text{C.2})$$

also shown in Fig. C.1. This timescale is compared to the total duration of the 3D simulation for each model. Due to the slow rotation of G20 the growth time of the MRI is longer than the simulated time in most of the simulated domain. For M13 the simulated time is long enough to capture multiple growth times in the regions where the MRI is spatially resolved, such as C1 and R2.

Appendix D: Evolution of the magnetic field near convective boundaries

The evolution of the magnetic field at convective boundaries provides a useful diagnostic of magnetic-flux exchange between turbulent and radiative regions. This is particularly relevant for simulations that excise part of the stellar interior or impose magnetic boundary conditions, since the field strength near convective-shell boundaries can influence the Maxwell stresses and, consequently, the direction and efficiency of AM transport. In our global models, these boundary fields are not prescribed externally, but evolve self-consistently as the convective shells interact with their neighbouring radiative layers. Here, we examine



multidimensional evolution is taken into account. Instead, magnetic flux transported and amplified in the convective layers can connect regions that were initially separated in the 1D magnetic-field prescription.

Fig. D.1: Evolution of the poloidal magnetic-field flux, normalised to its initial value, at selected convective boundaries for models G20 (left) and M13 (right). The three boundaries shown are the lower and upper boundaries of C1 and the lower boundary of C2, each tracked at fixed mass coordinate.

this evolution to assess whether the magnetic field near the shell boundaries is governed mainly by contraction and flux conservation, or whether it is also affected by local amplification and magnetic exchange with the turbulent regions.

To separate passive compression from genuine field amplification, we monitor the flux-freezing scaling expected for the poloidal component. For a radial or poloidal field component, flux freezing through a spherical surface implies $B_r r^2 \approx \text{const.}$

Figure D.1 shows the evolution of the poloidal magnetic-field flux, normalised to its initial value, at selected convective boundaries. We find clear amplification of the poloidal field at all boundaries. The boundaries of C1 approach a steady state by the end of the simulation, whereas the lower boundary of C2 has not yet reached a settled state. This is consistent with the slower development of turbulence in C2, discussed in Paper I, which indicates that this region requires more convective turnovers to reach a statistically stationary state.

The growth of the boundary field is not simply a passive consequence of contraction. As shown in Fig. 7, the magnetic field amplified inside convective regions interacts continuously with the surrounding radiative layers. Magnetic flux is transported across the convective–radiative interfaces, enhancing the field in the neighbouring radiative zones while also modifying the magnetic-field evolution inside the turbulent shells. This exchange may affect the saturation level reached in the convective regions and is therefore relevant for the resulting Maxwell stresses. Given the sensitivity of AM transport to magnetic-field strength, the self-consistent evolution of the field near convective boundaries can be important for determining the final AM profile of the progenitor.

Appendix E: 3D rendering of magnetic field lines

We visualise the 3D structure of the magnetic field lines of model M13 in Fig. E.1. Field lines rooted in the radiative core remain strongly wound around the rotation axis, consistent with the toroidal dominance found in the spectral analysis. Field lines rooted in the oxygen shell extend over a larger radial range and display a more tangled geometry, reflecting the stronger poloidal component and the multi-scale structure generated by turbulence.

This topology implies that the collapsing core and the surrounding burning shells are not magnetically isolated once the

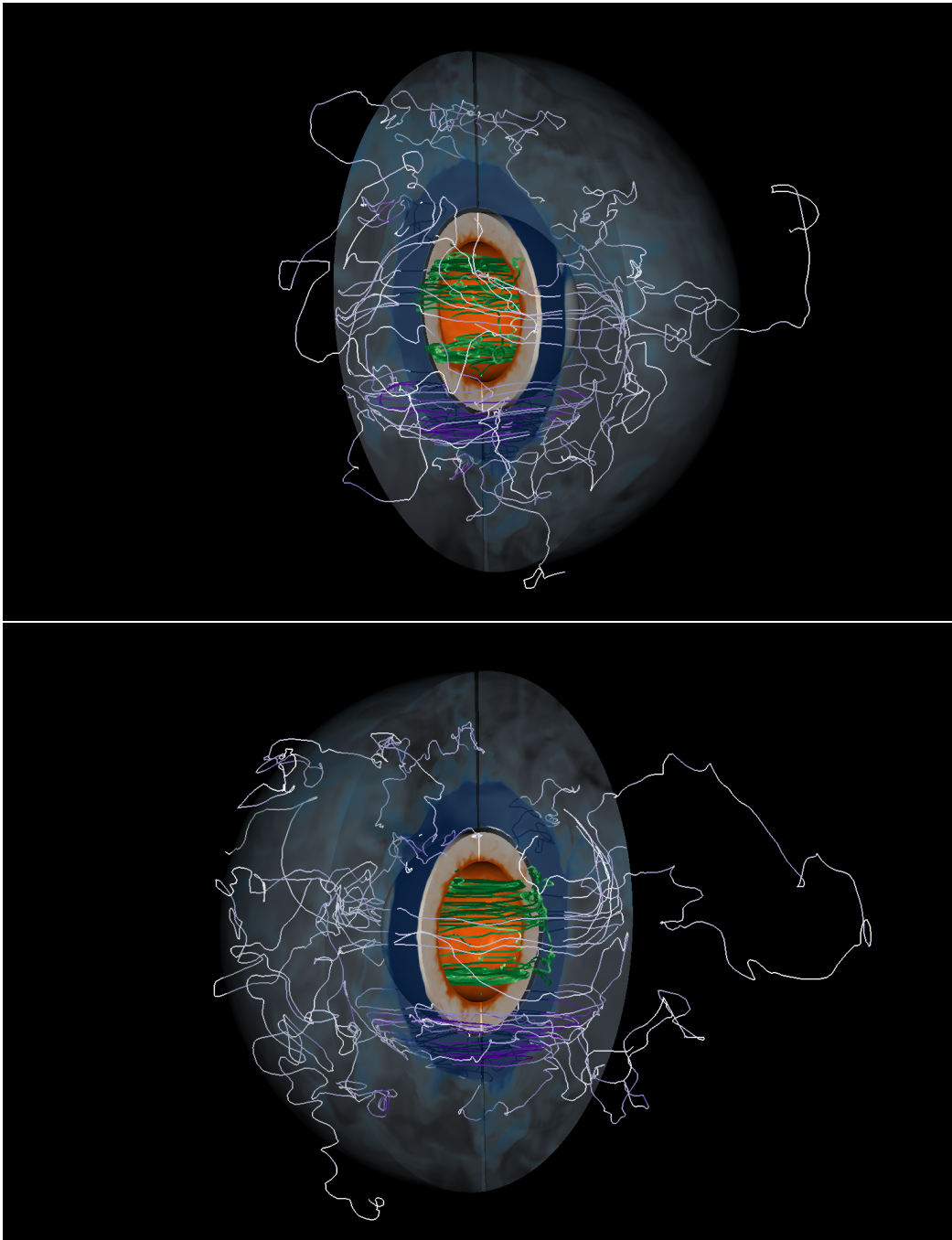


Fig. E.1: 3D rendering of the inner oxygen shell (blue shading) and silicon-rich region (orange shading) of model M13 at collapse. Magnetic field lines are traced from foot points located in the oxygen layer (purple lines) and inside the radiative iron core (green lines). The two panels show different viewing angles: right side view above and left side view below.